Journal of Magnetism and Magnetic Materials 446 (2018) 214–220

Contents lists available at ScienceDirect

Journal of Magnetism and Magnetic Materials

journal homepage: www.elsevier.com/locate/jmmm

Research articles

Sulfur doping effect on microstructure and magnetic properties of Nd-Fe-B sintered magnets

Fang Yang [a], Yan-li Sui [b], Cun-guang Chen [a], Si-Yang Ye [b], Ping Li [a], Zhi-meng Guo [a,*], Vladislav Paley [c], Alex A. Volinsky [c,*]

[a] *Institute for Advanced Materials & Technology, University of Science and Technology Beijing, Beijing 100083, China*
[b] *State Key Laboratory for Advanced Metals and Materials, University of Science and Technology Beijing, Beijing 100083, China*
[c] *Department of Mechanical Engineering, University of South Florida, Tampa, FL 33620, USA*

ARTICLE INFO

Article history:
Received 26 May 2017
Received in revised form 8 August 2017
Accepted 8 September 2017
Available online 9 September 2017

Keywords:
Nd-Fe-B sintered magnets
Coercivity
S
Grain boundaries
Grain refinement

ABSTRACT

In this paper, the effects of sulfur (S) doping on microstructure and magnetic properties of Nd-Fe-B sintered magnets were studied. With 0.2 wt% S doping, the melting point of the Nd-rich eutectic phases decreased from 1038 K to 1021 K. Clear and continuous grain boundary phases were also formed with smaller grain size. The average grain size was 7.83 µm, which was approximately 1.3 µm smaller than that of the undoped magnets. The coercivity enhancement was attributed to boundary microstructure modification and grain size optimization. The coercivity of the 0.2 wt% S-doped magnets increased from 15.54 kOe to 16.67 kOe, with slight changes of the remanence and the maximum magnetic energy production. The magnetic properties of the overdoped magnets deteriorated, due to the reduction in density and decrease of the volume fraction of the main phase. Globular S precipitates in the Nd-rich triple junctions were hexagonal Nd_2O_2S phase and tetragonal NdS_2 phase. S addition allows reducing Dy usage in magnets with comparable magnetic properties.

1. Introduction

Due to their high energy density, Nd-Fe-B sintered magnets have been applied in various fields [1,2]. However, the coercivity and the Curie temperature are too low for environmentally friendly applications in hybrid vehicles, electric vehicles, and wind power generators, where the required operating temperature is above 473 K [3–5]. At elevated temperatures, the effects of thermal activation on the reversal process are increased, which in turn decrease the coercivity [6,7]. Generally, partial substitution of Dy for Nd in the $Nd_2Fe_{14}B$ phase is effective to enhance the coercivity of Nd-Fe-B sintered magnets. $(Nd, Dy)_2Fe_{14}B$ has a higher magnetic anisotropy field, so Dy-containing magnets have higher coercivity when compared to Dy-free magnets [8]. However, there is a strong demand to reduce the usage of Dy from the highly coercive Nd-Fe-B sintered magnets because of high cost and the scarcity of the heavy rare earth elements. Furthermore, the heavy rare earth substitution leads to the decrease of produced energy [9,10]. Recently, many efforts have been undertaken to improve the coercivity of magnets without introducing Dy.

It is well known that coercivity is influenced not only by the magnetic anisotropy field of the $Nd_2Fe_{14}B$ phase, but also by the microstructure [11,12]. Coercivity can be enhanced by optimizing grain boundaries, lowering the melting temperature, and reducing the grain size [13–15]. According to previous work, the microstructure improvement can be achieved by the addition of non-rare earth elements. The grain growth inhibition can be achieved by the addition of Mo, W and Nb, due to the grain boundary pinning. The grain boundaries can be promoted with Al, Cu or Ga addition, because these elements reduce the melting point and improve wetting between the $Nd_2Fe_{14}B$ and Nd-rich phases [16–19]. Generally, sulfur (S) is thought to be an impurity element in most materials. Recently, demonstrations have shown that S powder addition is beneficial for coercivity enhancement [19–22]. Li et al. found that the coercivity of the MoS_2-added magnets was higher than the Mo-added magnets [20]. In the Dy/S co-doping magnets, S addition also produces a Dy-saving effect due to the suppressed formation of $(Nd, Dy)_xO_y$ phases in the triple junctions [21,22]. However, little information is available about the effects of S introduction on microstructure and magnetic properties of magnets, especially on melting point and grain size inhibition.

---

* Corresponding authors.
E-mail addresses: zmguo@ustb.edu.cn (Z.-m. Guo), volinsky@usf.edu (A.A. Volinsky).

https://doi.org/10.1016/j.jmmm.2017.09.023
0304-8853/© 2017 Elsevier B.V. All rights reserved.

In this work, we investigated the effect of S doping in Nd-Fe-B sintered magnets with respect to the melting point, grain size, distribution of grain boundaries and magnetic properties. In addition, the distribution of S element was systematically studied and the mechanism of coercivity enhancement with S introduction in the magnets was established. We compared its magnetic and microstructural properties with those of the S-free magnets.

2. Experimental procedure

The commercial Nd-Fe-B and S powders were used as the raw materials. The purity of the raw materials was over 99%. Nd-Fe-B powders (~5 μm) with a nominal composition of 31.0Re(Re-Nd, Pr)-0.5Dy-bal.Fe-1.0B-4.0M(wt%, M-Cu, Al, Co, Cr), were mixed with various amounts of commercially available sulfur (0.0, 0.1, 0.2, 0.3, 0.5 wt%) powders. This was done by ball milling for 1 h using SPEX-8000 mixer/mill with steel balls and a ball-to-powder weight ratio was 5:1. The average particle size of S powder was about 5 μm. After being pressed by die-upset in a magnetic field of 17 kOe, the green compacts were vacuum-sintered at 1323 K for 3 h. Subsequently, the magnets were annealed at 1203 K for 3 h and subsequently annealed at 758 K for 6 h.

The magnets were cut into cylindrical shapes with a dimensional size of Φ 8 × 5 mm^3 and mechanically polished. Density of the sintered magnets was determined by the Archimedes' principle measurement. The magnetic properties at room temperature of the processed magnets were measured by a magnetic measurement device (NIM-200C). Thermal analysis was performed using differential scanning calorimetry (DSC, NETZSCHSTA449) under protective Ar gas. Microstructural studies were conducted by field emission scanning electron microscope (FESEM, Supra55), operating at 15 kV. Average grain sizes and grain size distribution were evaluated by an image analyzer (UTHSCSA Image Tool). Phase composition and identification were performed using electron probe microanalysis (EPMA, JEOL, JXA-8230) and transmission electron microscopy (TEM, Tecnai G2 F30 S-TWIN) combined with energy dispersive spectroscopy detector (EDS, GENESIS) and selected area electron diffraction (SAED). The TEM analysis was carried out at 300 kV. In addition, thin foil specimens for the TEM analysis were prepared using an ion milling system.

3. Results and discussion

Table 1 and Fig. 1 show the corresponding magnetic performance for the S-free and S-doped magnets. The density of the undoped magnets is about 7.59 g/cm^3, while that of the 0.2 wt% S-doped magnets is 7.53 g/cm^3. When the S addition increased to 0.5 wt%, the density decreased to 7.42 g/cm^3. The density decreased with increasing S content, as summarized in Table 1. The measured coercivity H_{cj}, remanence B_r and maximum magnetic energy product $(BH)_{max}$ values of the S-free magnets are 15.54 kOe, 12.30 kGs, and 36.71 MGsOe, respectively. With 0.1 wt% S addition, the H_{cj} value increased to 16.03 kOe. When increasing the S content to 0.2 wt%, the coercivity reached its maximum value. The coercivity increased to 16.67 kOe, and the peak value was 7.3% higher than the S-free magnets. In addition, the Br decreased from 12.30 kGs to 11.95 kGs, and $(BH)_{max}$ changed from 36.71 MGsOe to 35.98 MGsOe. The introduction of S 0.2 wt% resulted in a slight decrease in B_r and $(BH)_{max}$. Upon further increasing S content to 0.5 wt%, the magnetic performance of the magnets significantly decreased. The coercivity decreased from 16.67 kOe to 15.12 kOe. The proper S addition is beneficial to enhance the coercivity in the magnets. However, excessive S addition leads to the deterioration in magnet density and magnetic properties due to pores formation.

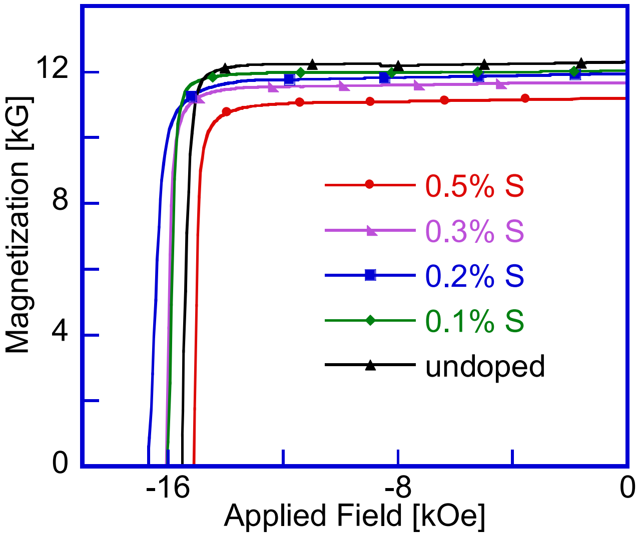

Fig. 1. Demagnetization curves for the undoped and S-doped magnets.

The microstructure changes and grain size distribution in the magnets with different S content are shown in Fig. 2. The dark gray regions are the $Nd_2Fe_{14}B$ main phases, and the bright regions correspond to the Nd-rich phases. The bright contrast of the grain boundaries suggests the existence of Nd-rich phases in the grain boundaries. The grain boundary phases (GBPs), in the undoped magnets, are discontinuous and not clearly visible, as seen in Fig. 2(a). This means that the Nd-rich phases are not connected well along the grain boundaries. In addition, the distribution of the main phase grains is not uniform. With S doping, grain boundaries of the magnets are changed in morphology, as seen in Fig. 2 (b) and (c). Compared to the S-free magnet, clearly visible and more continuous GBPs are observed in the 0.2 wt% S-doped magnets, isolating the $Nd_2Fe_{14}B$ grains. Thus, the surface defects at grain boundaries decreased, resulting in a suppression of the reversal domain nucleation at the GBPs which may deteriorate the coercivity. However, when increasing the S content to 0.5 wt%, there are many tiny defects along the grain boundaries, as seen in Fig. 2(c). Therefore, full densification cannot be easily achieved, as demonstrated by its low density of 7.42 g/cm^3.

In the undoped magnets, the average grain size is 9.14 μm which is relatively large, as seen in Fig. 2(d). In contrast, the grain

Table 1
Magnetic properties of the S-doped magnets as a function of the S content.

Sample	Density [g·cm^{-3}]	H_{cj} [kOe]	B_r [kG]	$(BH)_{max}$ [MGsOe]	H_k/H_{cj}
NdFeB	7.59±0.01	15.54	12.30	36.71	0.97
NdFeB + 0.1 wt%S	7.58±0.01	16.03	12.03	36.24	0.97
NdFeB + 0.2 wt%S	7.53±0.01	16.67	11.95	35.98	0.96
NdFeB + 0.3 wt%S	7.47±0.01	16.07	11.67	35.06	0.96
NdFeB + 0.5 wt%S	7.42±0.01	15.12	11.19	33.88	0.94

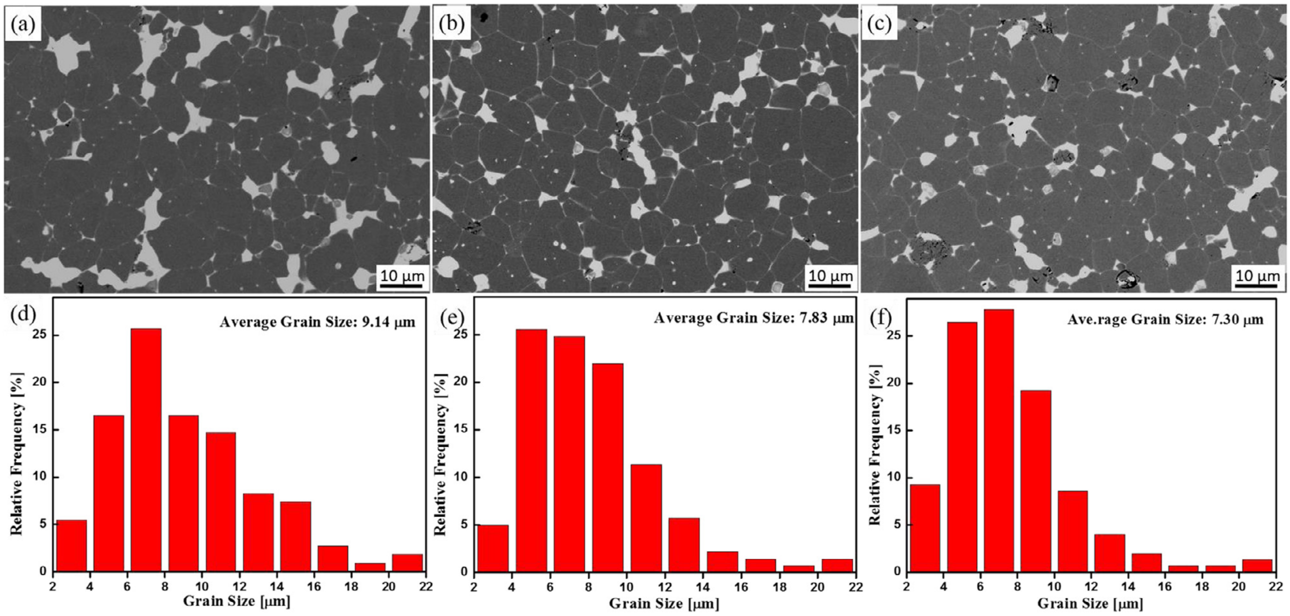

Fig. 2. Backscatter electron images and grain size distribution of: (a), (d) S-free; (b), (e) 0.2 wt% S-doped and (c), (f) 0.5 wt% S-doped magnets.

size is relatively small and the grain size distribution is more uniform in the S-doped magnets, as seen in Fig. 2(e) and (f). The average grain size for the 0.2 wt% S-doped magnets is 7.83 µm, while that for the 0.5 wt% S-doped magnets is 7.3 µm. Thus, the average grain size for the 0.2 wt% S-doped magnets is approximately 1.3 µm smaller than that of the undoped magnets. Therefore, grain refinement is achieved with S addition. As a result, distribution of the GBPs and grain size are optimized in the 0.2 wt% S-doped magnets, resulting in coercivity enhancement. However, there exist obvious defects, which may work against the magnetic performance when increasing the S content to 0.5 wt%. Excessive S doping leads to the deterioration in the magnetic properties. Most likely, the reduction of the magnetic properties occurred due to the decrease of the density and the decrease of the volume fraction of the main phase.

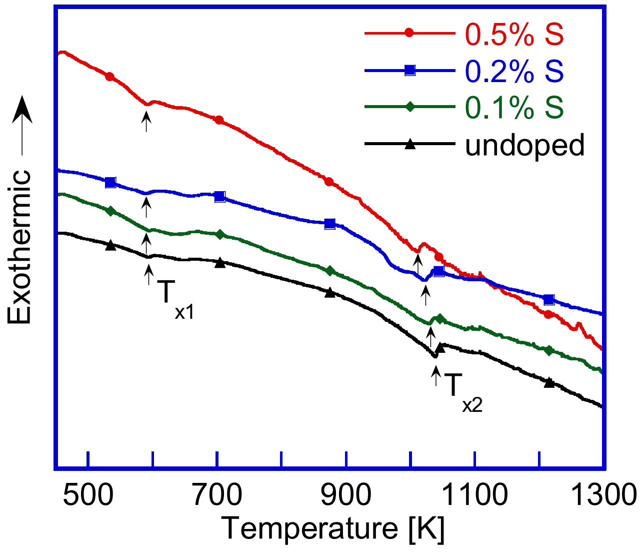

Fig. 3. DSC curves of Nd-Fe-B sintered magnets with different S additions.

Fig. 3 presents the DSC curves of Nd-Fe-B sintered magnets with different S content. The DSC analysis was performed from room temperature to 1323 K, at a constant heating rate of 0.67 K/s. Two endothermic peaks are observed on all DSC curves. The first endothermic peak, T_{x1}, corresponds to the Curie temperature of the $Nd_2Fe_{14}B$ phase, while the second endothermic peak, T_{x2}, corresponds to the melting point of the Nd-rich eutectic phases. During sintering, the Nd-rich eutectic phases primarily precipitate in a liquid formed at T_{x2}. Upon further heating, the liquid phases penetrate into the grain boundaries between the $Nd_2Fe_{14}B$ phases. Therefore, the wettability between the main phases and the Nd-rich phases plays an important role on the microstructure and magnetic properties. Compared with the undoped magnets, T_{x1} remained about the same in the S-doped magnets and, the Curie temperature was around 600 K. The melting point, T_{x2} for the 0.2 wt% S-doped magnets decreased from 1038 K to 1021 K. Upon further increasing S content to 0.5 wt%, the melting point of the magnets can be significantly decreased. Meanwhile, the melting point decreases to 1011 K, and the value is actually lower than that of the S-free magnets by about 27 K. This suggests that the melting temperature is lowered with S addition, as shown in Fig. 3. With the addition of low melting-point elements, the liquidus temperature was reduced, resulting in the wettability improvement and the formation of uniform and continuous of GBPs [23]. Therefore, the melting point reduction with S doping, may be the main factor, which caused the optimization of the GBPs and grain size distribution. It can be inferred that S addition promotes the uniformity and continuity of GBPs because it reduces the melting point and improves wettability.

Fig. 4 shows the BSE image and EDS patterns of the 0.2 wt% S-doped magnets. EDS analysis presents the composition difference between the Nd-rich phases. The EDS result proved that the dark gray region (spot “A”) corresponds to the $Nd_2Fe_{14}B$ phases. Two types of Nd-rich phases can also be recognized in Fig. 4(a): one with a uniform white contrast, and the other with a slightly gray contrast in the triple junctions. The former (spot “B”) is found to correspond to the NdO_x oxide phase, and the latter (spot “C”) is found to be NdO_xS_y oxysulfide phase. The greyly contrasted oxysulfide phase appears as a globular inclusion, which looks similar to the oxide phase. The new oxysulfide phases exist in the Nd-rich

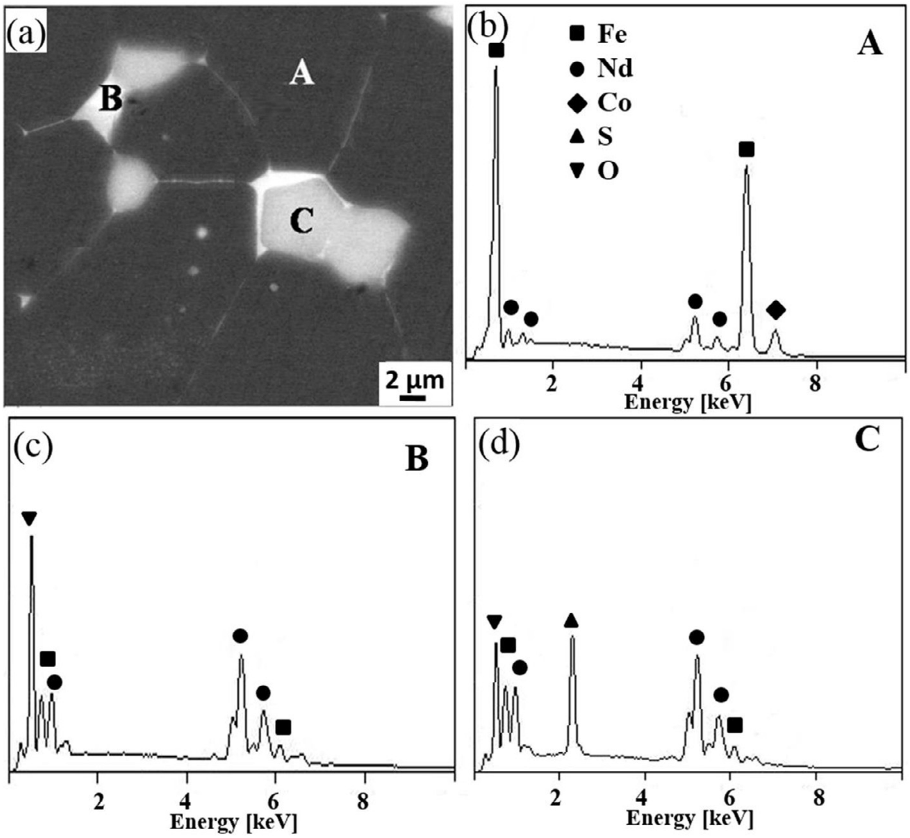

Fig. 4. (a) SEM images and the corresponding EDS patterns: (b) for the region A; (c) for the region B and (d) for the region C.

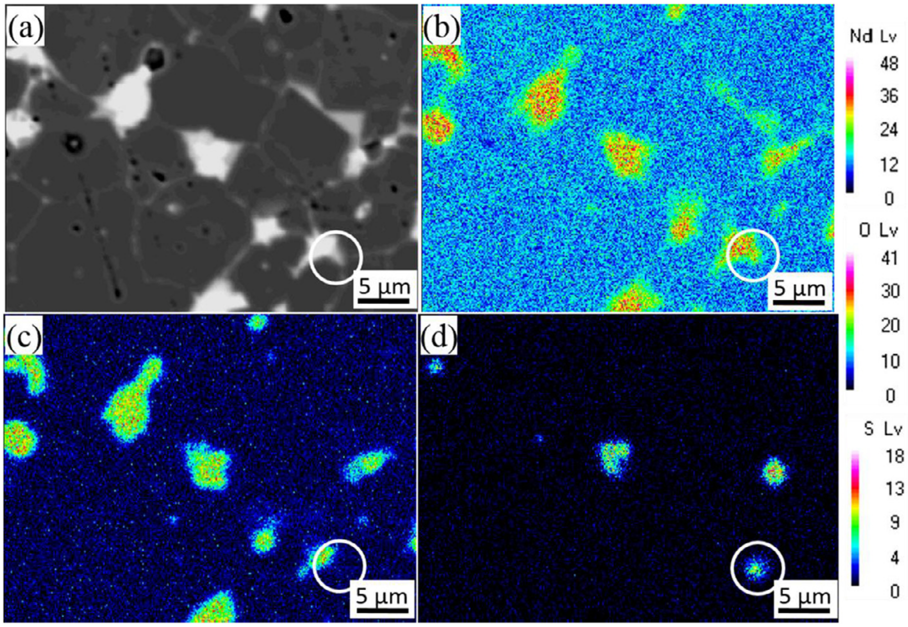

Fig. 5. SEM image and EPMA maps of Nd, O and S elements of the magnets with 0.2 wt% S addition: (a) SEM backscattered electron image; (b) Nd element; (c) O element, and (d) S element.

triple junction regions of the 0.2 wt% S-doped magnets. To further confirm the distributions of S-containing precipitates, the distribution of Nd, O, and S elements was conducted by the EPMA, as shown in Fig. 5. It can be observed that Nd is dominant in the intergranular phase, and O is also enriched. Both Nd and O elements are the essential components of the Nd-rich phases at the triple junctions. The Nd-rich phases may be composed of several different phases, depending on the O content. Commonly reported phases are dhcp-Nd, fcc-NdO_x, and hcp-Nd_2O_3 [8]. The S distribution in the magnets is not uniform, as seen in Fig. 5(d). In addition, the

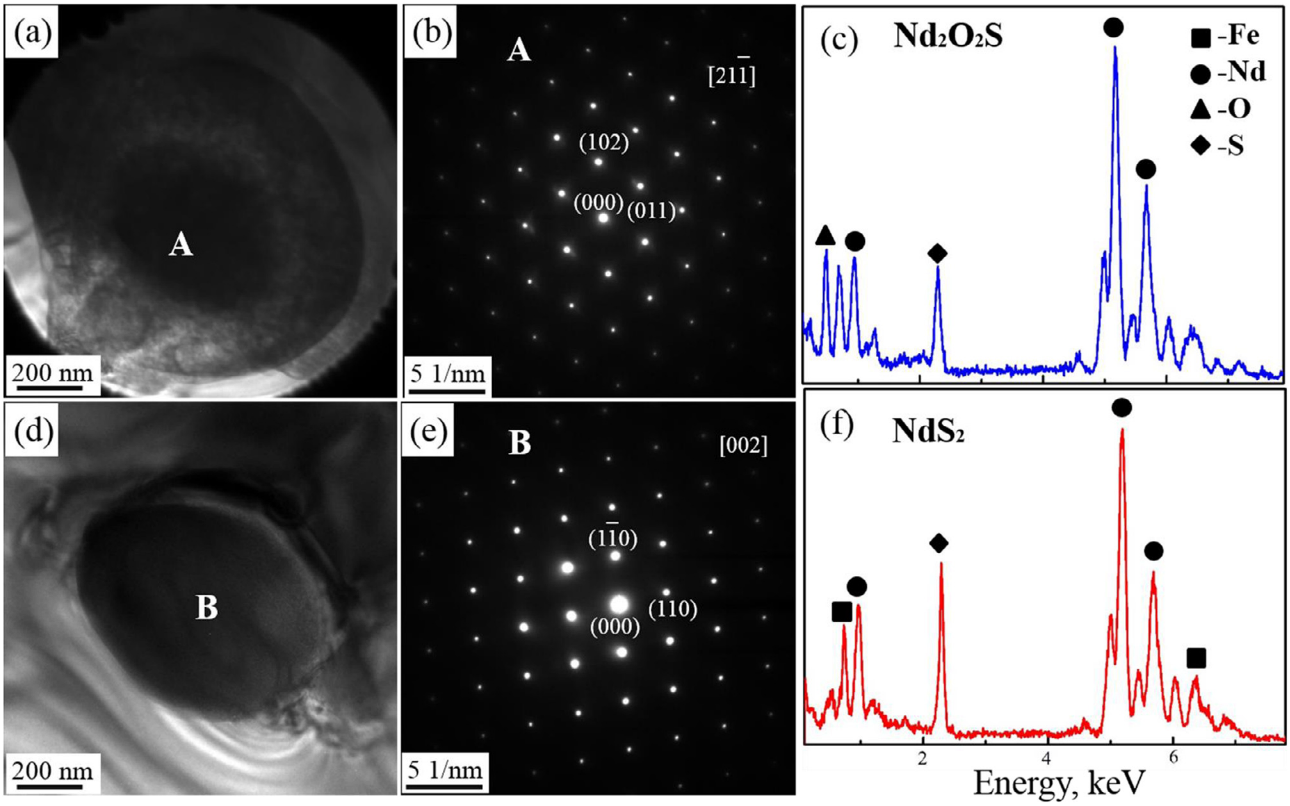

Fig. 6. TEM images (a) and (d), SAED and EDS patterns from region: (b), (c) A; (e), (d) B in the 0.2 wt% S-doped magnets.

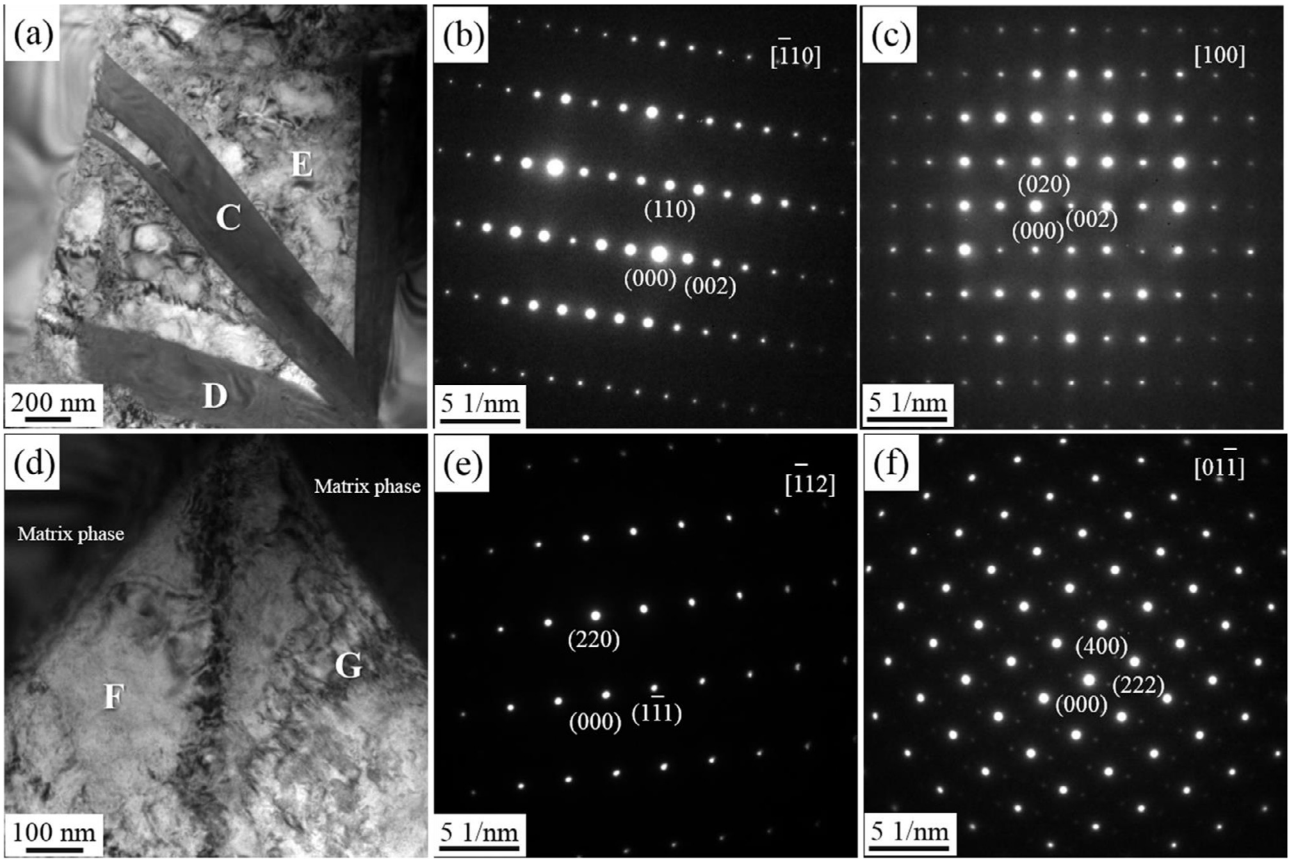

Fig. 7. (a), (d) Bright-field TEM images of intergranular Nd-rich phases in the 0.2 wt% S-doped magnets, SAED patterns for regions: (b) C; (c) E; (e) F, and (f) G.

Table 2
Composition of the Nd-rich phase in Fig. 7 determined by EDS (relative at.%).

Region	Fe [at.%]	Nd [at.%]	O [at.%]	Structure
C	7.4	84.9	7.7	dhcp
D	4.0	85.8	10.2	dhcp
E	4.7	79.8	15.5	fcc
F	5.9	75.8	18.3	fcc
G	6.3	67.5	26.2	$Ia\bar{3}$

S-containing precipitates are formed mostly in the Nd-rich triple junctions, completely overlapping the Nd distribution. There is no O in parts of the S-rich regions, just like the white mark shows in Fig. 5(d). It can be inferred that the potential phase of S element in the S-rich region might be NdS_x or NdO_xS_y, depending on the S content [24].

Fig. 6 shows the TEM bright field images, SAED, and EDS patterns of the S-rich phases in the 0.2 wt% S-doped magnets. Both Nd_2O_2S phase "A" and NdS_2 phase "B" are observed in the globular precipitates at the triple junctions. The SAED patterns revealed that regions "A" crystallized in a hexagonal structure with a = 0.395 nm, and c = 0.679 nm [25], as shown in Fig. 6(b). The measured distances from (000) to (011), (102) are 0.195 nm and 0.244 nm, respectively. The zone axis is identified as $[21\bar{1}]$. The hexagonal structure is corresponding to the Nd_2O_2S phase, with space group $P\bar{3}m1$. At the same time, another SAED pattern (Fig. 6(e)) revealed that the S-rich phase in region B is a tetragonal structure with space group P4/nmm. The measured distances from (000) to (110), $(1\bar{1}0)$ are 0.290 nm and 0.285 nm, respectively. It can be identified as NdS_2 phase with lattice parameters of a = 0.402 nm, and c = 0.803 nm [26]. The EDS patterns in Fig. 6 compares two spectra acquired in regions "A" and "B". In the NdS_2 phase, the O peak is much lower than that in the Nd_2O_2S phase, whereas the S peak is much higher. Microstructural observation proves that the S-containing precipitates can be Nd_2O_2S or NdS_2 phase in the S-doped magnets.

Fig. 7 compares the different crystal structures of the intergranular Nd-rich phases in the 0.2 wt% S-doped magnets. SAED patterns were obtained at five locations in the intergranular phases, marked with "C" to "G". The results of the composition analysis for different regions in Fig. 7 are listed in Table 2. Fig. 7(b) shows that the regions "C" and "D" have a low O content and are identified as dhcp-Nd phases with lattice parameters a = 0.366 nm, and c = 1.180 nm [27]. In addition, the measured distance from (000) to (002) is 0.588 nm, whereas the distance from (000) to (110) is 0.183 nm. It can be inferred that the dhcp-Nd phases appear as a slab inclusion. Region "E" consists of fcc-NdO_2 with space group $Fm\bar{3}m$ with the lattice parameter a = 0.554 nm, as seen in Fig. 7(c). And, the measured distances are 0.275 nm and 0.277 nm, respectively. The zone axis is identified as [400]. At the same time, another SAED pattern was obtained from the region "F", with the zone axis $[\bar{2}24]$ and the corresponding distances are 0.319 nm and 0.195 nm. It can also be indexed as the fcc-NdO_2 type [28]. The SAED pattern in Fig. 7(f) revealed that the Nd-rich phase in region "G" is fcc-Nd_2O_3 with space group $Ia\bar{3}$ [29], whose O content is about 26.2 at.%. The measured distances from (000) to (222), (400) are 0.318 nm and 0.273 nm. It has been reported that the presence of $Ia\bar{3}$ phase, with the unit cell parameter a = 1.108 nm, is a general case in Nd-Fe-B sintered magnets [4]. There exists a significant difference in Nd and O contents between different Nd-rich phases, as shown in Table 2. The O distribution is non-uniform. The dhcp-Nd phase consists of low O content, which is likely to be a solid solution of O in Nd metal. When the O content is between 11 at.% and 43 at.%, the crystal structure of the Nd-rich phases is found to be of the fcc type [30]. The Nd-rich phases appear as fcc-NdO_2 phase with 15–18 at.% O content, as show in Table 2.

Fig. 8 shows the TEM and HRTEM image of the GBPs in the 0.2 wt% S-doped magnets. Clearly visible and continuous GBPs can form a thin homogeneous grain boundary layer. The corresponding HRTEM images shows that the GBPs are crystalline, as shown in Fig. 8(b). Since the grain boundary layer of the GBPs is relatively thick (~10 nm), it was possible to determine the composition with EDS analysis. The EDS result confirmed that the GBPs in region "H" are Nd-rich phases. No sulfur peak can be identified in the EDS pattern. The S element is mainly enriched in the Nd-rich phases at triple junctions, as shown in Fig. 5.

The evident coercivity enhancement of the Nd-Fe-B sintered magnets with 0.2 wt% S addition is achieved. The melting point of the Nd-rich eutectic phases is lowered with S doping, as shown in Fig. 3, thus improving the wettability and fluidity of the liquid Nd-rich phase during sintering [20]. It has been reported that the presence of a large amount of the liquid phase increases the number of abnormal grain nuclei causing them to impinge upon each other and inhibiting the grain growth [31]. As a result, the microstructure of the 0.2 wt% S-doped was optimized. Clear and continuous GBPs are observed in the S-doped magnets. The average grain size is 7.83 μm, approximately 1.3 μm smaller than that for the undoped magnets. Therefore, a coercivity enhancement of 7.3% was obtained in the 0.2 wt% S, due to the smaller grain size and formation of the clear and continuous GBPs. Excessive S doping causes the sharp decrease in magnetic properties. Obvious defects

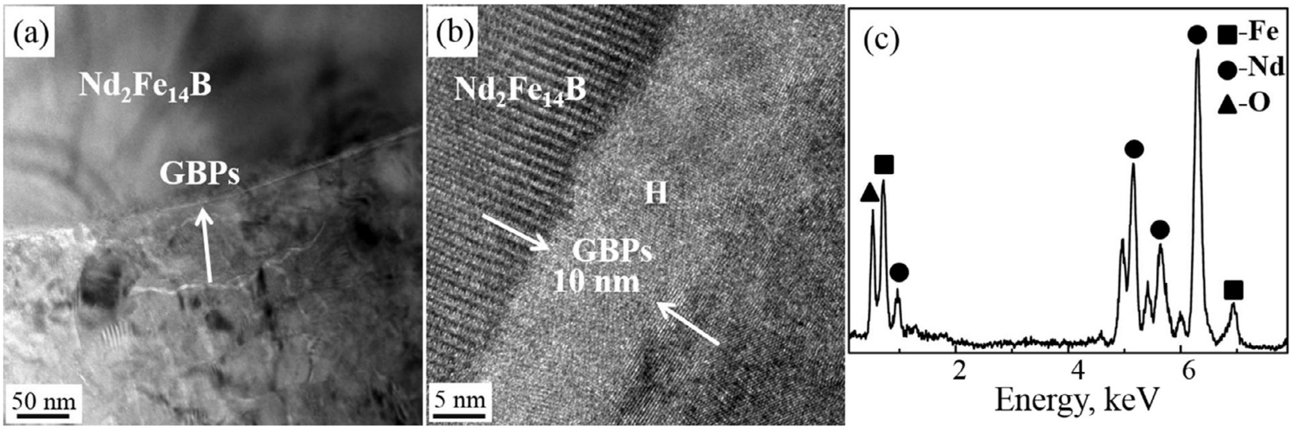

Fig. 8. (a) TEM, (b) HRTEM images and (c) EDS patterns from regions H in the 0.2 wt% S-doped magnets.

are observed along the GBPs, as shown in Fig. 2(c). In addition, the density of the S is about 2 g/cm^3, far below the density of the magnets. The deterioration of the magnetic properties might correlate with the rapid decline in density and the decrease of the volume fraction of the main phase.

The S element is mainly enriched in Nd-rich triple junctions, as shown in Figs. 4 and 5, forming the Nd_2O_2S or NdS_2 phase. The S distribution is also not uniform. The Nd-rich phases play an important role in the magnetic properties. The results show that the crystal structure of the Nd-rich phases is different with different Nd and O contents, as seen in Fig. 7. The slab inclusions (Fig. 7 (a)) are the dhcp-Nd phase with low O content (<11 at.%). When increasing the O content, the Nd-rich phases display an fcc structure. The fcc Nd-rich phases have better wettability with the $Nd_2Fe_{14}B$ main phase [4]. In the 0.2 wt% S-doped magnets, the fcc Nd-rich phases can be composed of NdO_2 or Nd_2O_3 phase, depending on the O content.

4. Conclusions

We have characterized the magnetic properties and microstructure of the S-doped Nd-Fe-B sintered magnets. The liquidus temperature is lowered with increasing S content, leading to the wettability improvement and grain refinement. The average grain size and grain size distribution are optimized in the 0.2 wt% S-doped magnets. As a result, the coercivity of the 0.2 wt% S doping magnets is 16.67 kOe, 7.3% higher than that of the S-free magnets. There is no notable decrease in the remanence and the maximum magnetic energy product. In the S-doped magnets, parts of the oxides are replaced by the Nd_2O_2S or NdS_2 phase in the triple-junction regions. A variety of chemical composition and crystal structure of the Nd-rich oxides are observed. The Nd-rich phases consist of dhcp-Nd, fcc-NdO_2 and fcc-Nd_2O_3 phases.

Acknowledgment

We gratefully acknowledge funding from the State Key Lab of Advanced Metals and Materials (No. 2013-ZD05).

References

[1] O. Gutfleisch, M.A. Willard, E. Bruck, C.H. Chen, S.G. Sankar, J.P. Liu, Magnetic materials and devices for the 21st century: stronger, lighter, and more energy efficient, Adv. Mater. 23 (2011) 821–842.

[2] Y. Matsuura, Recent development of Nd-Fe-B sintered magnets and their applications, J. Magn. Magn. Mater. 303 (2006) 344–347.

[3] X.L. Liu, X.J. Wang, L.P. Liang, P. Zhang, J.Y. Jin, Y.J. Zhang, T.Y. Ma, M. Yan, Rapid coercivity increment of Nd-Fe-B sintered magnets by $Dy_{69}Ni_{31}$ grain boundary restructuring, J. Magn. Magn. Mater. 370 (2014) 76–80.

[4] T.H. Kim, S.R. Lee, S. Namkumg, T.S. Jang, A study on the Nd-rich phase evolution in the Nd-Fe-B sintered magnet and its mechanism during post-sintering annealing, J. Alloys Compd. 537 (2012) 261–268.

[5] K. Hono, H. Sepehri-Amin, Strategy for high-coercivity Nd-Fe-B magnets, Scripta Mater. 67 (2012) 530–535.

[6] S. Bance, J. Fischbacher, T. Schrefl, Thermally activated coercivity in core-shell permanent magnets, J. Appl. Phys. 117 (2015) 821–842.

[7] K. Loewe, C. Brombacher, M. Katter, O. Gutfleisch, Temperature-dependent Dy diffusion processes in Nd-Fe-B permanent magnets, Acta Mater. 83 (2015) 248–255.

[8] T.G. Woodcock, O. Gutfleisch, Multi-phase EBSD mapping and local texture analysis in NdFeB sintered magnets, Acta Mater. 59 (2011) 1026–1036.

[9] U.M.R. Seelam, T. Ohkubo, T. Abe, S. Hirosawa, K. Hono, Faceted shell structure in grain boundary diffusion-processed sintered Nd-Fe-B magnets, J. Alloys Compd. 617 (2014) 884–892.

[10] S. Park, T.H. Kim, S.R. Lee, S. Namkung, T.S. Jang, Effect of sintering conditions on the magnetic and microstructural properties of Nd-Fe-B sintered magnets doped with DyF_3 powders, J. Appl. Phys. 111 (2012), 7A707–7A7073.

[11] T.T. Sasaki, T. Ohkubo, K. Hono, Structure and chemical compositions of the grain boundary phase in Nd-Fe-B sintered magnets, Acta Mater. 115 (2016) 269–277.

[12] W.F. Li, T. Ohkubo, K. Hono, Effect of post-sinter annealing on the coercivity and microstructure of Nd-Fe-B permanent magnets, Acta Mater. 57 (2009) 1337–1346.

[13] J.W. Kim, S.H. Kim, S.Y. Song, Y.D. Kim, Nd-Fe-B permanent magnets fabricated by low temperature sintering process, J. Alloys Compd. 551 (2013) 180–184.

[14] F. Vial, F. Joly, E. Nevalainen, M. Sagawa, K. Hiraga, K.T. Park, Improvement of coercivity of sintered NdFeB permanent magnets by heat treatment, J. Magn. Magn. Mater. 242–245 (2002) 1329–1334.

[15] D.W. Scott, B.M. Ma, Y.L. Liang, C.O. Bounds, The effects of average grain size on the magnetic properties and corrosion resistance of NdFeB sintered magnets, J. Appl. Phys. 79 (1996) 5501–5503.

[16] W.K. Jin, W.S. Lee, J.M. Byun, S.H. Kim, Y.D. Kim, Grain refinement in heavy rare earth element-free sintered Nd-Fe-B magnets by addition of a small amount of molybdenum, J. Appl. Phys. 117 (2015) 17B523.

[17] W.H. Cheng, W. Li, C.J. Li, X.M. Li, The role of Nb addition in Nd-Fe-B sintered magnets with high performance, J. Alloy Compd. 319 (2001) 280–282.

[18] S. Pandian, V. Chandrasekaran, G. Markandeyulu, K.J.L. Lyer, K.V.S. Rama-Rao, Effeet of Al, Cu, Ga, and Nb additions on the magnetic properties and microstructural features of sintered NdFeB, J. Appl. Phys. 92 (2002) 6082–6086.

[19] K.H. Bae, S.R. Lee, H.J. Kim, M.W. Lee, T.S. Jang, Effect of WS_2/Al co-doping on microstural and magnetic properties of Nd-Fe-B sintered magnets, J. Alloys Compd. 673 (2016) 321–326.

[20] W.F. Li, A.M. Gabay, M. Marinescu-Jasinski, J.F. Liu, C. Ni, G.C. Hadjipanayis, Microstructure of sintered ND-Fe-Ga-B magnets with Mo and MoS_2 addition, J. Magn. Magn. Mater. 324 (2012) 1391–1396.

[21] A.M. Gabay, M. Marinescu, W.F. Li, J.F. Liu, G.C. Hadjipanayis, Dysprosium-saving improvement of coercivity in Nd-Fe-B sintered magnets by Dy_2S_3 additions, J. Appl. Phys. 109 (2011) 083916.

[22] F. Yang, L.C. Guo, P. Li, X.Z. Zhao, Y.L. Sui, Z.M. Guo, X.X. Gao, Boundary structure modification and magnetic properties of Nd-Fe-B sintered magnets by co-doping with Dy_2O_3/S powders, J. Magn. Magn. Mater. 429 (2017) 117–123.

[23] J. Fidler, J. Bernardi, T. Schrefl, Permanent magnets-New microstructural aspects, Scripta Mater. 33 (1995) 1781–1791.

[24] M. Ohta, H. Yuan, S. Hirai, Y. Uemura, K. Shimakage, Preparation of R_2S_3(R:La, Pr, Nd, Sm) powders by sulfurization of oxide powders using CS_2 gas, J. Alloys Compd. 374 (2004) 112–115.

[25] ICDD PDF Card No. 00-027-0321.

[26] ICDD PDF Card No. 00-026-1278.

[27] ICDD PDF Card No. 00-065-5015.

[28] ICDD PDF Card No. 00-046-1074.

[29] ICDD PDF Card No. 00-065-3184.

[30] M. Wenjian, Z. Lanting, L. Qiongzhen, S. Aidang, W. Jiangsheng, K. Matahiro, Dependence of the crystal structure of the Nd-rich phase on oxygen content in an Nd-Fe-B sintered magnet, Scripta Mater. 59 (2008) 179–182.

[31] H.Y. Park, C.W. Ahn, H.C. Song, J.H. Lee, S. Nahm, K. Uchino, H.G. Lee, H.J. Lee, Microstructure and piezoelectric properties of $0.95(Na_{0.5}K_{0.5})NbO_3$-$0.05BaTiO_3$ ceramics, Appl. Phys. Lett. 89 (2006) 062906.